Accepted Manuscript

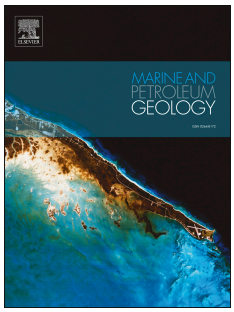

Geophysical evidence for structurally-controlled, authigenic carbonate cementation in the Laminaria High, Bonaparte basin, Northwest Shelf of Australia

Lamees Abudlkareem, Jonathan Imber, Richard Hobbs

PII: S0264-8172(18)30424-0

DOI: 10.1016/j.marpetgeo.2018.10.018

Reference: JMPG 3530

To appear in: *Marine and Petroleum Geology*

Received Date: 28 June 2017

Revised Date: 8 October 2018

Accepted Date: 12 October 2018

Please cite this article as: Abudlkareem, L., Imber, J., Hobbs, R., Geophysical evidence for structurally-controlled, authigenic carbonate cementation in the Laminaria High, Bonaparte basin, Northwest Shelf of Australia, *Marine and Petroleum Geology* (2018), doi: https://doi.org/10.1016/j.marpetgeo.2018.10.018.

Geophysical evidence for structurally-controlled, authigenic carbonate cementation in the Laminaria High, Bonaparte basin, Northwest Shelf of Australia

Lamees Abudlkareem[a,b] , Jonathan Imber[b], Richard Hobbs[b]

[a] Department of Earth Sciences, Baghdad University, Al-Jadriya Street, Baghdad, Iraq

[b] Department of Earth Sciences, Durham University, Durham DH1 3LE, UK.

E-mails: l.n.abdulkareem@durham.ac.uk

jonathan.imber@durham.ac.uk

r.w.hobbs@durham.ac.uk

Abstract:

3D seismic reflection data are ussssed to investigate the processes which have led to the development of amplitude anomalies on reflectors in the faulted, Cenozoic overburden on the Laminaria High, Northwest Shelf of Australia. Amplitude and root mean square (RMS) attributes are mapped on two reflectors (seabed and horizon H9) that were deposited synchronous with fault activity and are located adjacent to predominantly ENE-WSW striking fault traces. On the seabed, the main anomaly is located on the up-dip side of the fault trace, and is elongated parallel to the local time structure contours. These observations are consistent with the anomalies having developed in response to structurally-controlled fluid seepage along, and up-dip migration away from the fault trace. The other amplitude anomalies associated with the H9 reflector are also located adjacent to fault traces but are discordant to the local time structure contours. The latter observation is inconsistent with the migration of buoyant fluid at the present day; instead, it suggests that the anomalies may be due to cemented hardgrounds that formed due to seepage when the faults intersected the palaeo-seafloor but were subsequently buried and deformed during

ongoing sedimentation and fault growth/linkage. Prominent anomalies mapped on reflectors within the pre-faulting succession (H10) are located adjacent to, and are elongated along, sub-seismic scale, NW-SE striking faults or, as in the case of a deeper horizon (H13) show no clear relationship with the faults. We conclude that there is no relationship between the occurrence of anomalies and the magnitude of throw, or the duration of activity, along the Cenozoic faults. The results suggest that whilst fluid seepage and cementation were structurally-controlled, these processes were also influenced by permeability variations that cannot be resolved by seismic interpretation methods.

Keywords:

Pliocene to Recent fluid migration
Amplitude anomalies
Laminaria High
Bonaparte Basin

1. Introduction

Hovland (1990) demonstrated a close association between carbonate build ups (reef formation) and active hydrocarbon seeps at the seafloor. The seeps provide sources of energy and carbon for bacterial communities. Specifically, authigenic carbonate is a result of the aerobic oxidation of methane, which creates a favorable ecosystem for the precipitation of carbonate hardgrounds (Barens and Goldberg, 1976; Blumenberg et al. 2015). Evidence for such authigenic carbonate cementation has been widely documented, for example, in the North Sea (e.g. Hovland et al., 1987; Hovland, 2002, Schroot et al., 2005), Porcupine Basin (e.g. Hovland et al., 1994) and on the Northwest Shelf of Australia (e.g. O'Brien and Woods, 1995; O'Brien et al., 1999; Cowley and O'Brien, 2000; O'Brien

et al.,2002; Howarth and Alves, 2016; Van Tuyl et al., 2018). The present study uses 3D seismic reflection data to evaluate the spatial and temporal relationships between authigenic carbonate cementation and Pliocene-Recent fault activity on the Laminaria High, Northwest Shelf of Australia.

The Laminaria High lies within the Timor Sea and includes numerous oil and gas accumulations (Smith et al., 1996). These accumulations are typically found within Jurassic reservoirs in the footwalls of Mesozoic, rift-related normal faults (Whittam et al., 1996). However, several traps were found to be dry, or to contain only residual hydrocarbon columns (De Ruig et al., 2000; Abbassi et al., 2015). Complete or partial trap failure was caused by transtensional reactivation of these rift-related normal faults during late Miocene-Pliocene oblique collision between the Australian plate and the SE Asian plate (De Ruig et al., 2000). Gartrell et al. (2006) found that intact traps are preserved where the fault closure (at the depth of the reservoir) is provided by a structure with < 60 m of post-rift, Miocene-Pliocene throw. Trap failure occurs where the bounding fault segment has a high post-rift throw (> 80 m). Gartrell et al. (2005, 2006) proposed a trap integrity model in which hydrocarbons from breached or partially breached traps migrate upwards towards the seabed along major faults that cut the Cenozoic overburden.

Previous authors working on seismic reflection profiles from the Yampi Shelf (ca. 300 km south-southwest of the Laminaria High) have identified a correlation between high amplitudes on the seabed reflector and features that relate to active hydrocarbon seepage, including carbonate hardgrounds (areas of enhanced cementation on the sea floor) (Rollet et al., 2006). O'Brien et al. (1999) described similar high amplitude anomalies associated with Eocene strata within the shallow subsurface of the Vulcan sub-basin, ca. 150 km southwest of the Laminaria High. These authors integrated interpretations of the seismic reflection profiles with geochemical analyses of samples obtained from boreholes. They

proposed that co-migration of hydrocarbons and high-salinity brines through the Cenozoic fault network resulted in isotopically-light carbonate cementation that, in turn, produced high acoustic impedance contrasts with the surrounding, less well-cemented sediments (O'Brien et al., 1999).

Langhi et al. (2010) noted the presence of amplitude anomalies on the seabed reflector and other shallow horizons on the Laminaria High. Here, the distribution of amplitude anomalies is strongly controlled by the Cenozoic fault network and, in some cases, the anomalies are associated with hydrocarbon flags along some of the Cenozoic fault planes (Langhi et al., 2010). These observations, and the similarity with the seismic anomalies reported elsewhere on the Northwest Shelf (e.g. O'Brien et al., 1999; O'Brien and Woods, 2005; Rollet et al., 2006), led Langhi et al. (2010) to propose that the amplitude anomalies associated with seismic reflectors on the Laminaria High are the result of hydrocarbon seeps and associated authigenic carbonate cementation along fault planes.

In our study, we will test Langhi et al.'s (2010) hypothesis that the seismic anomalies on the seabed reflector and in the shallow subsurface result from authigenic carbonate cementation. Specifically, this study investigates the relationships between the amplitude anomalies, the present-day structure, and active faults that intersected the palaeo-seabed at different times during the deposition of the syn-faulting, Pliocene-Pleistocene succession. We utilise 3D seismic reflection dataset calibrated with exploration wells from the AC/P8 permit area on the Laminaria High to carry out detailed structural mapping and to characterise the distributions of amplitude and RMS (root mean square) anomalies in the shallow subsurface. Our results are consistent with Langhi et al's (2010) hypothesis, and demonstrate the importance of small-, in addition to large-throw faults in controlling hydrocarbon (re-) migration and authigenic carbonate cementation within the Cenozoic overburden on the Laminaria High.

2. Background

2.1. Tectonic and structural setting:

The Laminaria High is located in the northern part of the Bonaparte Basin, near the southern edge of the Timor Trough (Figure 1a). It is bordered by the Nancar and Cartier troughs to the south and by the Flamingo Syncline to the east (Charlton et al., 1991 Smith et al., 1996) (Figure 1b). The Laminaria High appears to lie within a broad "hinge" zone, where the structural trend changes from NE-SW to the south, to ENE-WSW to the north (Figure 1b).

The structural history of the Bonaparte Basin is complex and is characterised by three rifting phases during the Palaeozoic–Mesozoic eras (Whittam et al., 1996): 1) a NW–SE rifting phase associated with faulting that initiated during the Late Cambrian, and subsequent reactivation during the Late Devonian to Early Carboniferous; 2) a Neotethys rifting phase, which is responsible for the thin crust of the Bonaparte Basin and took place during the Late Carboniferous to the Early Permian; and 3) a Late Jurassic-rifting phase, caused by the breakup of Gondwana. During the Cenozoic, the geological evolution of the Laminaria High has been dominated by the ongoing collision between the Australian plate and the Southeast Asian plate, which happened in two stages. The first stage started ca. 8 Ma during the late Miocene. The second stage began during the Pliocene, about 3-4 Ma, with deformation accommodated by reactivation of pre-existing faults. Fault activity decreased during the Pleistocene (Whittam et al., 1996; Baillie et al., 1994; Keep et al., 2002).

The structural trend of the Laminaria High is E-W to ENE-WSW. The direction of the present-day maximum horizontal stress (S_{Hmax}) is NNE-SSW, sub-perpendicular to the regional fault strike (de Ruig et al., 2000) (Figure 1a). For the purposes of this study, the

key structures that accommodated Mesozoic to Neogene extension on the Laminaria High are: 1) a set of ENE-WSW striking, Jurassic-Cretaceous horst and graben structures; and 2) a set of mainly ENE-WSW striking, Neogene normal faults that initiated above the reactivated Mesozoic structures (Shuster et al., 1998; Gartell et al., 2006; Langhi et al., 2010) (Figure 2a). A deeper set of E-W striking, Permian horsts underlies the area (Langhi et al., 2008), but are too deep to be imaged within our 3D seismic volume, and are not considered further here.

2.2. Stratigraphy

The stratigraphy of the Laminaria High is described in detail by Smith et al. (1996). The hydrocarbon reservoir section is within the Laminaria Formation, which is Callovian to Oxfordian in age. The Laminaria Formation consists of massive sandstone with minor interbedded claystone. Open marine shales of the Frigate (Oxfordian–Kimmeridgian), Flamingo (Tithonian-Berriasian) and Echuca Shoals (Valanginian-Barremian) formations represent the seal through which any deep-sourced hydrocarbons must have migrated to reach the shallow subsurface. The Lower and Upper Cretaceous are represented by the Bathurst Island Group, above which the lithology changes from dominantly clastic sequences into the carbonate-dominated sequence represented by the Johnson, Hibernia, Prion and Cartier formations (Palaeocene to Oligocene). The Miocene to Pleistocene Oliver and Barracouta formations include calcarenites and calcilutites, which are the shallowest sedimentary rocks within the study area, and represent an extensive cover of prograding shelf carbonate deposits (Smith et al., 1996) (Figure 1c).

2.3. Hydrocarbon charge history

The main source rocks in the Laminaria High include shales of the Plover, Laminaria, Frigate and Flamingo formations (Smith et al., 1996; George et al., 2004). The initial

charge of oil and gas occurred during the Late Jurassic to Early Cretaceous, followed by the main phase of oil charge during the Middle to Late Eocene. A later phase of oil and gas charge is suggested to have occurred from the Miocene onward (Wittham et al., 1996). Most of the drilled traps show evidence of residual oil, confirmed by geochemical and petrophysical analysis of core samples (Abbassi et al., 2015). This observation is consistent with the traps having been breached, and the hydrocarbons having leaked.

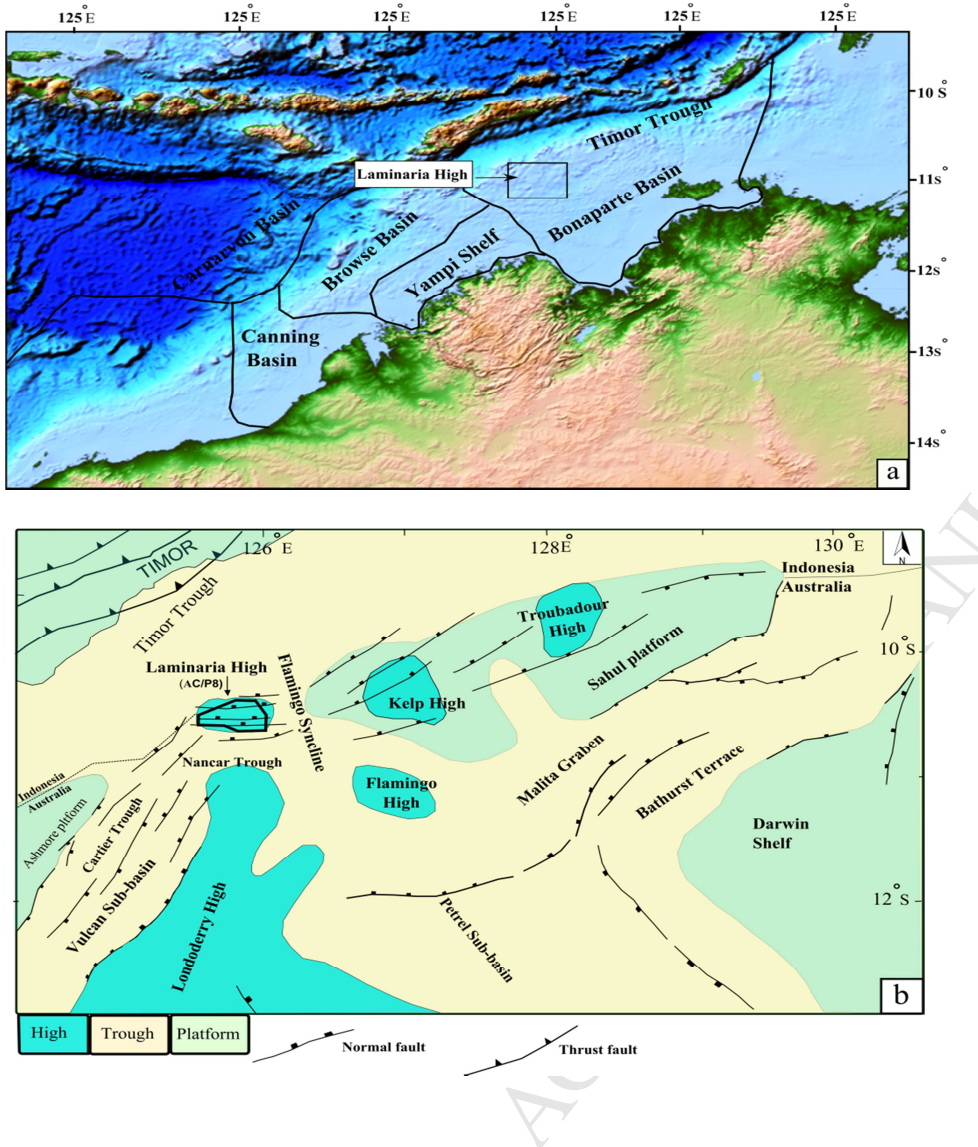

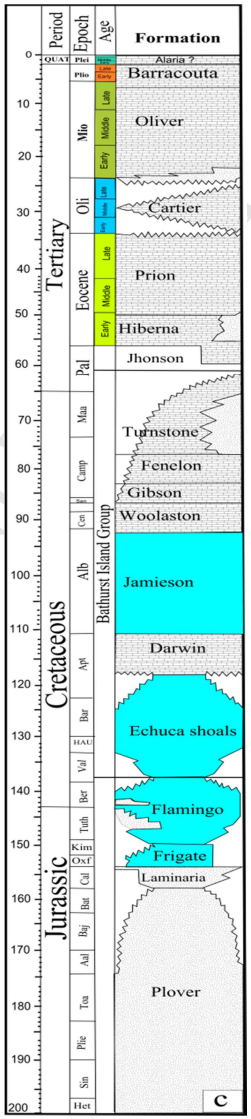

Figure 1. (a) Topographic and bathymmetric map of the main basins on the Northwest Shelf of Australia. Elevation and depth data provided by Geoscience Australia (2018). **(b)** Geological setting and Jurassic structure map of northwestern Bonaparte Basin, modified from Long and Imber (2012). **(c)** Generalized stratigraphic column for the Laminaria High (modified from De Ruig et al., 2000).

3. Data and methodology

3.1. Data

The dataset used in this study is a three-dimensional (3D), time migrated seismic volume supplied by Geoscience Australia. These data were acquired in 1995 within the AC/P8 permit block over the Laminaria High, which has an area of approximately 760 km^2 (Figures 1a and 1b). The data were shot in E-W direction; the bin dimensions are 12.5 m (inline) × 12.33 m (crossline). A series of seismic processing steps were applied on this volume which includes: true amplitude recovery, FK filter, deconvolution and DMO (dip moveout) correction. Velocity analysis (NMO) was applied to the pre-stack data, which were then CDP stacked followed by the 3D post-stack time migration. An example of a north-south section extracted from the volume is shown in Figure 2. The data as provided by Geoscience Australia have a bias of about -6; the positive impedance seabed reflection shows a zero-phase wavelet with a larger negative central lobe that confirms the polarity of data is negative (Langhi et al., 2011). In our interpretation, we used this volume to map seismic reflectors (Horizons H1-H13) and faults, the regional dip of the seabed and sediment thickness (Brown, 2011). Depth conversion was not applied to the whole volume as a reliable velocity model was not available, but given the consistency of the stratigraphy across the volume, we believe that depth conversion would have minimal effect on fault and horizon geometries (Long and Imber, 2012). Check shots from well Alaria-1 (Figures 2a and b) are used to calibrate the seismic horizons to the geological formations of the study area. (Note: for the rest of the paper we refer to all of the horizons using the letter “H” followed by a number (e.g. H9 for horizon H9),

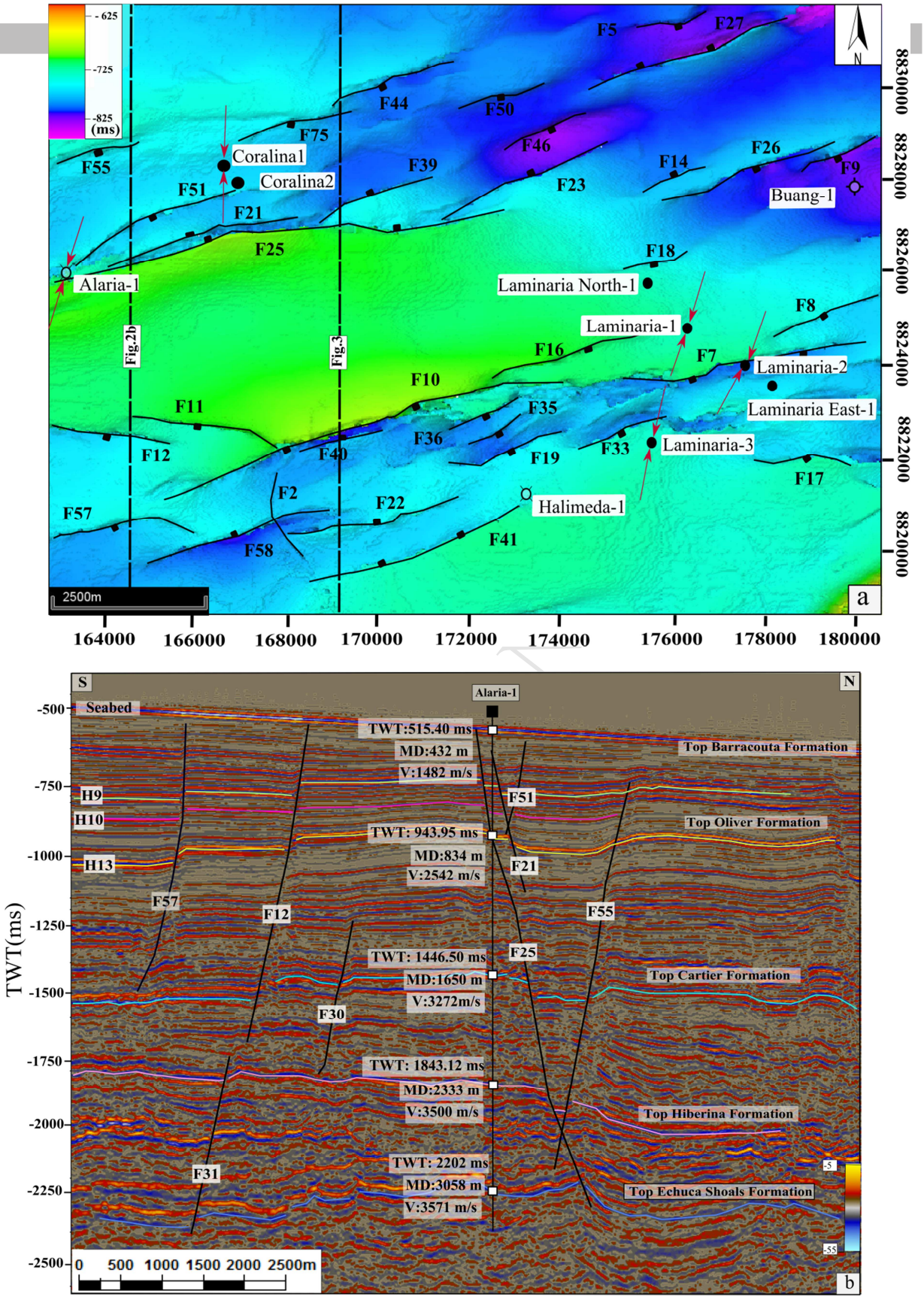

Figure 2. (a) Two-way time (TWT) structural map of horizon H9 showing the main structural elements and well locations. The locations of the seismic sections shown in Fig. 2 (a) and in Fig. 3 are indicated. Red arrows are the direction of the maximum horizontal stress (SHmax) and are taken from De Ruig et al. (2000). Note that the cartographic reference system is Universal Transverse Mercator (UTM) Zone 52S. **(b)** Seismic profile (cross line no. 2545) showing the interpreted horizons and faults. Note formation tops and checkshots are from well Alaria-1.

3.2. Methodology

3.2.1. Horizon interpretation

In this study, we focus on four key horizons in the shallow subsurface: the seabed, horizon H9, horizon H10 and horizon H13 (Figure 2b), which are characterised by bright, sub-parallel and laterally continuous seismic reflectors. Manual interpretation was followed by 3D autotracking to infill the interpreted horizons. Additionally, a further 10 horizons (H1, H2, H3, H4, H5, H6, H7, H8, H11 and H12) were interpreted in the subsurface in order to constrain the throw distributions along active faults (section 3.2.2). We extract the amplitude (i.e. the absolute amplitude of the tracked seismic reflection event) along the seabed reflector and along subsurface horizons H9, H10 and H13 in order to investigate spatial variations in seismic amplitude. Such variations imply changes in the velocity and/or density of the sediments, and provide a qualitative indication of changes in lithology and fluid content.

3.2.2 Fault interpretation

Faults were manually picked in the 3D seismic volume, and correlated on time slices to obtain an accurate fault framework model. The locations of faults were then compared with the locations of amplitude anomalies on the seabed and other interpreted horizons, in order to test for potential structural control on the spatial distribution and shape of the amplitude anomalies. Figure 3 shows the main geometry of the faults in the study area.

According to Childs et al. (2003), throw contours drawn on a strike projection of a growth fault will be approximately vertical within the pre-faulting sequence, and approximately horizontal within the syn-faulting sequence. This contour pattern arises because the down-dip throw gradients are high relative to the lateral gradients within the syn-faulting succession. Therefore, the boundary between the sub-vertical and the sub-horizontal contours separates

the pre- and syn-faulting regions of a fault surface (Childs et al., 2003). Horizon surfaces and faults were exported from Petrel® to TrapTester®. We combine each fault surface with the interpreted horizons to generate fault polygons defined by the hanging-wall and footwall cut-off lines along each fault surface. Then, we use functionality within TrapTester® to compute the throw attribute for each fault and, finally, generate throw contour maps for each fault plane.

3.2.3. Seismic attribute analysis

We extract the root mean square (RMS) amplitudes along the seabed reflector and along the key horizon surfaces (H9, H10 and H13) within a window that extends 20 ms above and below the key horizons. The RMS amplitude attribute is useful to highlight isolated amplitude anomalies and can be used to track changes in lithology and/or fluid content (e.g. Chen and Sidney, 1997). For example, Simm and Bacon (2014) showed the consistency between an RMS amplitude anomaly associated with a hydrocarbon flat spot, and the structure contours associated with a 4-way dip closure. We use a similar approach in our study. Specifically, the migration of buoyant fluids (e.g. hydrocarbons) is controlled by the local and regional subsurface structure: the flow direction is towards structural highs, i.e. up-dip, perpendicular to the time (or depth) structure contours. In addition, fluid contacts are controlled by local spill points, which are again determined by the structure contours. We therefore investigate the relationship between the two-way time (TWT) structure contours and the amplitude and RMS anomalies on key horizons within the Cenozoic succession.

We also utilised the edge detection and spectral decomposition seismic attributes (e.g. Brown, 2011). These attributes were extracted along selected horizon surfaces to highlight subtle structural and stratigraphical features. The edge detection attribute is based on the calculation of the local dip for the seismic event (Luo et al., 1996). This attribute identifies

discrete edges on a horizon surface, which might be related to the presence of minor (small-throw) faults and increases the confidence in our structural interpretation. The spectral decomposition (SD) attribute helps to delineate subtle features at a specific frequency (Partyka et al., 1999; Othman et al., 2016). For example, when hydrocarbons replace water in porous sediments it attenuates the frequency response of the seismic reflector. Langhi et al. (2010) used an SD map of the seabed reflector to support their interpretation of the seismic anomalies on the Laminaria High. Below, we compare the SD attribute extracted along the seabed within our seismic volume with Langhi et al's (2010) SD map.

4. Results

4.1. Seabed

4.1.1. Amplitude

The amplitude map is characterised by two distinct families of anomalies. The brightest amplitude anomalies are elongated in a ENE-WSW direction and are developed adjacent to the ENE-WSW striking faults that intersect the seabed reflector (Figure 4). The second group of anomalies is somewhat dimmer. These anomalies are elongated in a NW-SE direction, approximately perpendicular to the TWT structure contours, and appear to be cross-cut by the fault traces (Figure 4 – arrow).

The brightest amplitude anomaly on the seabed map (< 7 km in length) is associated with F10 and ranges from -27 to -33 (Figure 4). The anomaly is located on the hanging-wall side of F10 and is elongated parallel to the TWT structure contours. In the vicinity of F10, the seabed reflector dips towards the northwest; thus the hanging-wall side of the fault lies up-dip of the footwall side (Figure 3).

Smaller seabed amplitude anomalies (< 2.5 km in length; Figure 4) also appear along F11 and F12, within the amplitude range of -25 to -30, all on the hanging-wall side of these faults. Fault F7 is associated with an amplitude anomaly ranging between -25 and -27, in the vicinity of the Laminaria-1, 2 and the Laminaria East wells (which discovered oil). Moderate seabed amplitude anomalies exist along a series of small, ENE-WSW striking faults F19, F33, F35 well (dry and off structure) (Figure 4). The northern part of the seabed amplitude map shows no obvious seismic anomalies along faults F25, F23 and F39 in the vicinity of the Alaria-1 well (which was dry and off-structure), or the Coralina-1 and 2 wells (which discovered oil) (Figure 4).

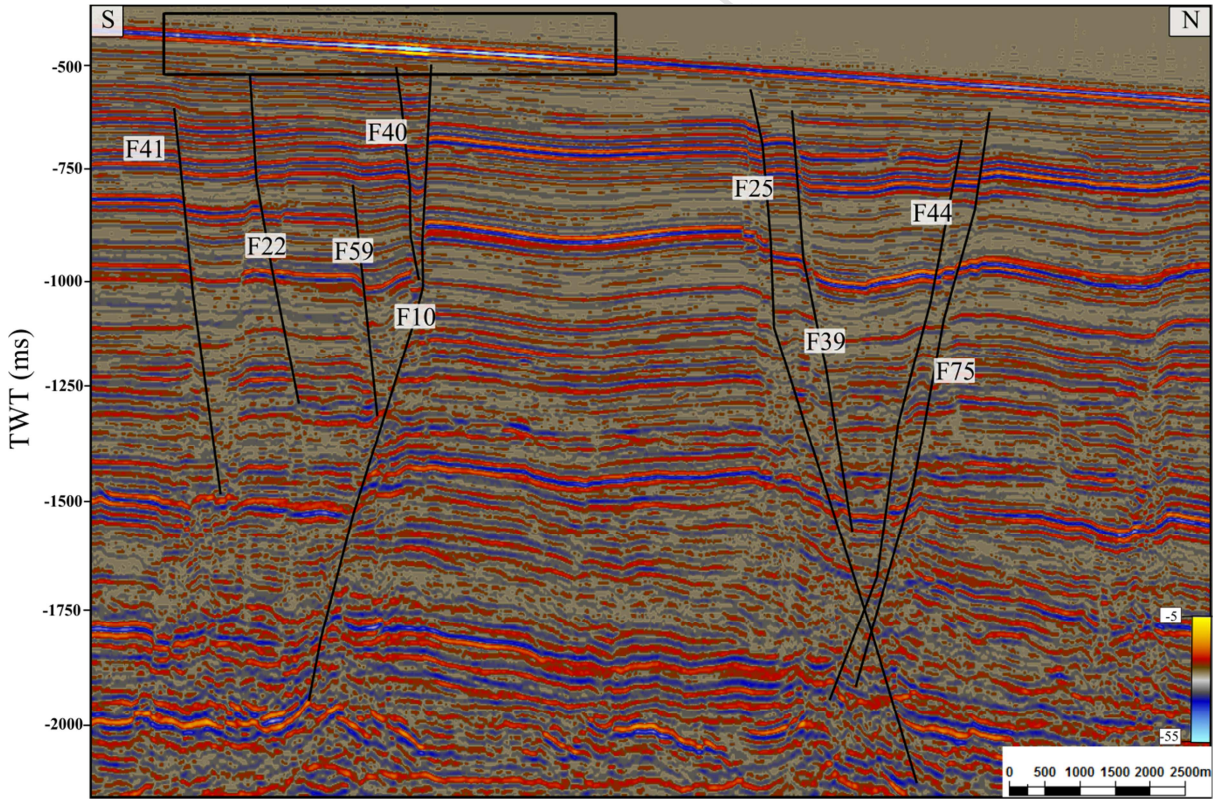

Figure 3. Seismic profile (cross line no. 2325) showing the geometry of the main faults in the study area. Note the amplitude anomaly at the seabed associated with fault F10 (box). Location of the seismic profile is shown in Figures 2a and 4.

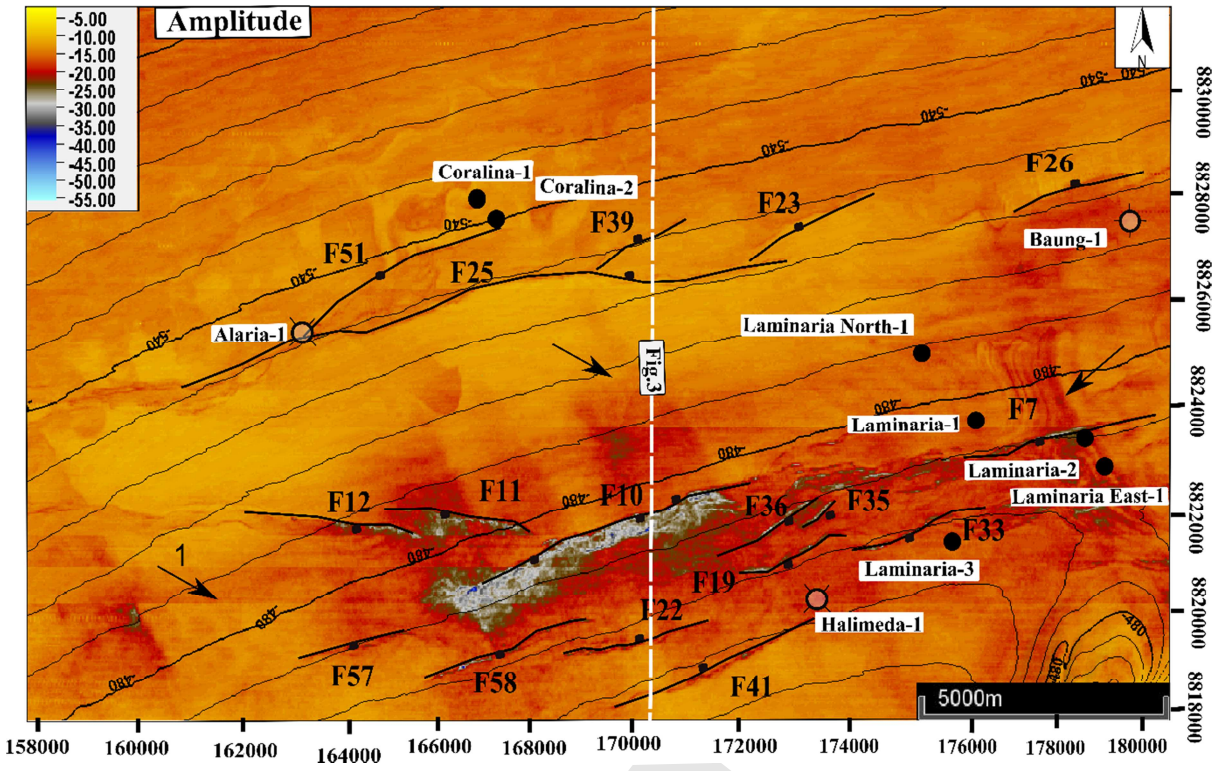

Figure 4. Amplitude map for the seabed. The two-way time structure contours are shown. The map shows high negative amplitude anomalies associated with sets of normal faults F7, F10, F11, F12, F19, F35 and F36 in the southern part of the study area. Note the lack of amplitude anomaly associated with fault F25 in the northern part of the area. Well locations are presented on this map (off structure/breached wells (dry) ☼, oil discovery well ● ,breached well/dry ☼). East-west striping in the amplitude map is a footprint of the original E-W acquisition geometry as shown by arrow1. The origin of the low amplitude anomalies to the north of F25 is unknown.

4.1.2. RMS amplitudes

The RMS amplitude map highlights similar features (Figure 5). Again, the brightest anomalies occur within the hanging-wall of F10, with smaller RMS anomalies being associated with F7, F11, F12, F19, F33, F35 and F36. The second family of anomalies identified on the amplitude map is slightly less prominent on the RMS amplitude map (Figure 5).

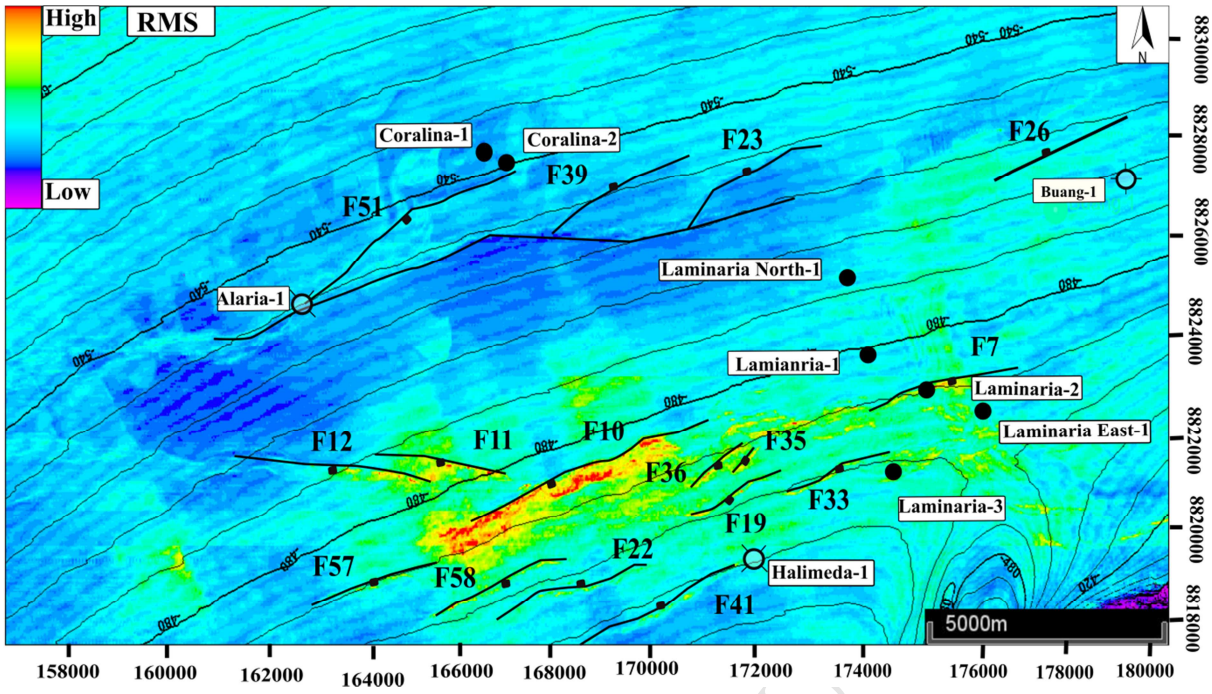

Figure .5. RMS amplitude map for the seabed showing a similar distribution of anomalies as shown in Figure 4. The two-way time structure contours for this horizon are shown. The principal RMS amplitude anomalies are associated with sets of normal faults F7, F10, F11, F12, F19, F35 and F36 in the southern part of the study area.

4.1.3. Spectral decomposition attribute

Three frequency volumes (30Hz, 45Hz, and 80Hz) are generated using the spectral decomposition (SD) attribute. SD maps for the seabed were extracted from each volume. The amplitude map obtained from the 30Hz SD volume (Figure 6a) shows very similar features to those observed in the amplitude and RMS amplitude maps (Figures 4 and 5), although the SD attribute enhances the appearance of the bright spots compared with the amplitude map (Figure 4). For example, the SD map shows the anomaly along F58 more clearly compared to the equivalent amplitude anomaly in Figure 4.

At the seabed, we note that our SD results are different from the previous study reported by Langhi et al. (2010). The SD map from our survey shows that the high amplitude anomalies are only associated with the faults in the southern part of the survey (Figure 6a). In contrast,

the Langhi et al. (2010) study shows high amplitude anomalies along their "F1" array (Langhi et al.'s fault numbers) (Figure 6b) near well Alaria-1. Furthermore, amplitude anomalies exist along F11 and F12 in our SD map (Figure 4a), but there are no corresponding anomalies along "F4" (Langhi et al's fault numbers) in Langhi's SD map (Figure 4b). We suggest a possible reason for these differences in results is that the Langhi et al. (2010) study used a merged seismic volume that is composed of five different seismic surveys. It is possibly that matching filters, necessary to equalise the amplitude and frequency content of the input surveys, may have created artefacts. In our work, we used only one seismic survey that covers our study area. Therefore, we have not applied any additional frequency manipulation other than that applied to the original seismic volume as supplied by Geoscience Australia.

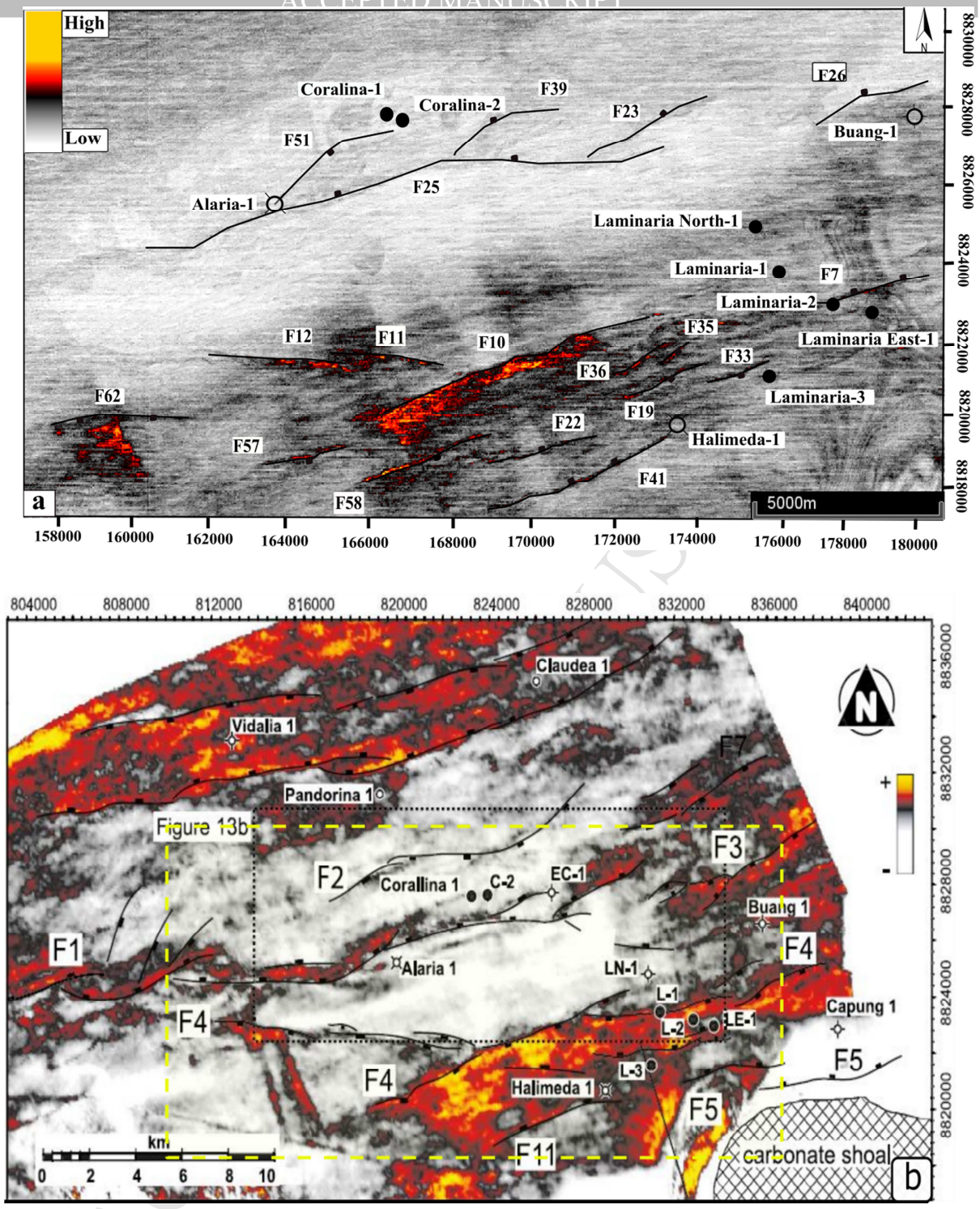

Figure 6. (a) A 30Hz spectral decomposition map extracted from the seabed horizon showing the fault traces and well locations. SD anomalies, indicated by the hot colours, are associated with the major faults in the southern part of the study area. **(b)** Spectral decomposition map at 30 Hz for the seabed (from Langhi et al. (2010) authorised by the AAPG Journal). This map shows a different distribution of SD anomalies compared to **(a)**. The yellow dashed box is the area covered by Figure 6a. Note the difference in x axis coordinates, Langhi et al. (2010) used a different Universal Transverse Mercator (UTM) projection, also note the fault numbering schemes are different between the two plots.

4.2. Horizon H9

4.2.1. Amplitude

Horizon H9 lies within the Barracouta Formation (Figure 1c). The amplitude map (Figure 2.7a) shows that amplitude anomalies exist in the footwalls of F7, F10, and F11 (in contrast to those on the seabed, which exist on the hanging-walls along the same faults). The amplitude anomaly associated with F10 (maximum throw of 106 ms on this horizon) ranges from -12 to -14 and is elongated in a NNW-SSE direction, discordant to the local TWT structure contours. Furthermore, the brightest parts of this anomaly do not coincide precisely with the footwall crest (Figures 7a and 1b-arrow).

The amplitude anomaly along F12 becomes dim and exists only at the eastern tip of the fault. Here, the amplitude anomaly ranges between -12 and -14. An amplitude anomaly exists along F11 and is connected with the anomaly that appears at the eastern tip of F12. F7 is also associated with an amplitude anomaly, which ranges from -12 to -13, and lies adjacent to the point of maximum throw (65 ms) in the hanging-wall of this fault (Figure 7a). This anomaly is elongated in an N-S direction and is again discordant to the local TWT structure contours.

Fault F25 has a maximum throw of 108 ms along H9, but the amplitude anomaly is much smaller in extent and less bright compared to the main anomaly along F10. In contrast to the seabed, there are significant anomalies along fault traces F44 and F75, which range from -12 to -14. The shape of these anomalies is complex; the brightest anomaly to the north of F44 is elongated in a NNE-SSW direction and is discordant to the local TWT structure contours (Figure 7a). In contrast, the slightly less distinct anomaly in the footwall of F75, at least locally, follows the structure contours (Figure 7a).

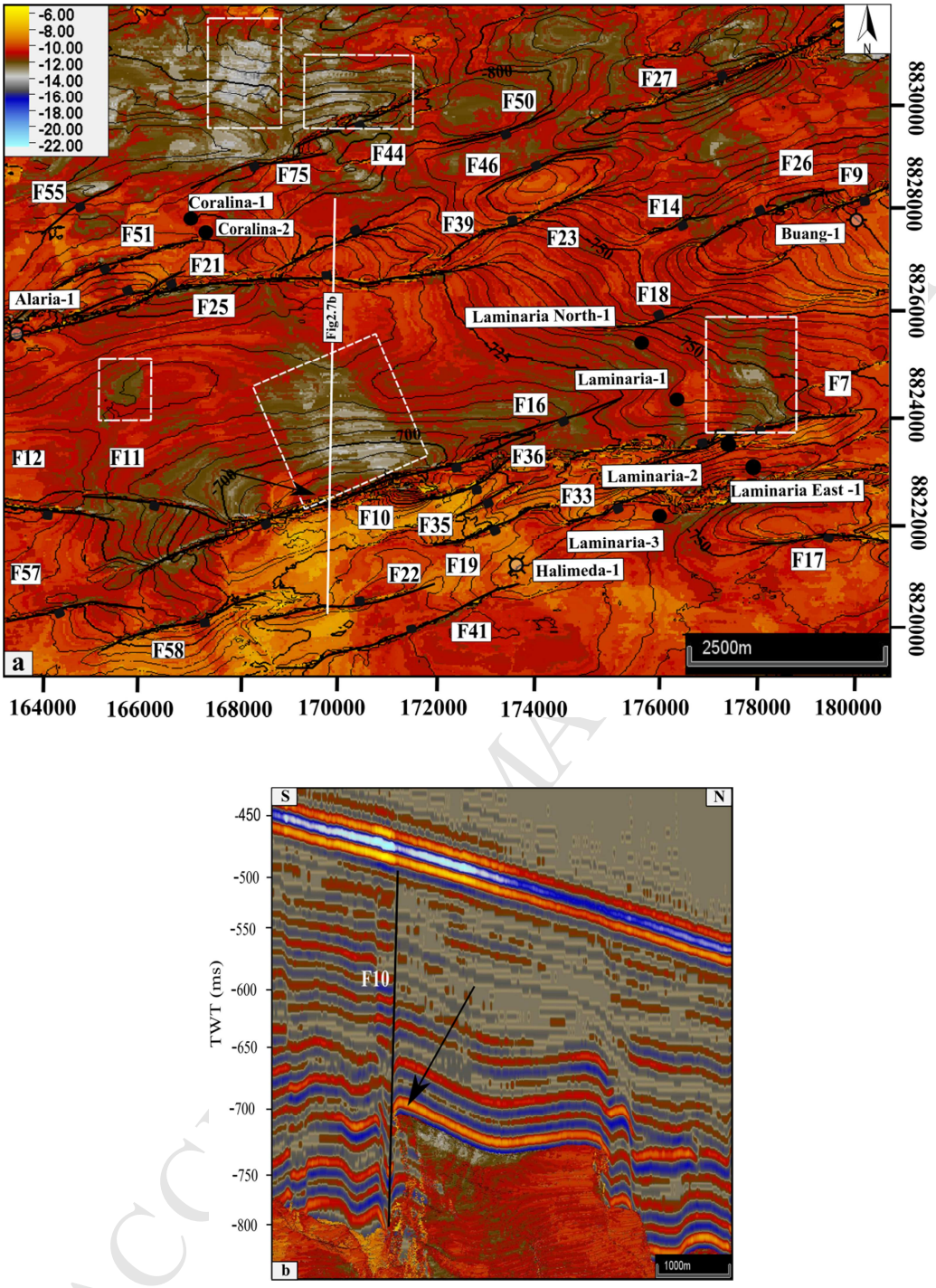

Figure 7. (a) Amplitude map for H9, overlain by the two-way time structural contours for this horizon. The map shows high negative amplitude anomalies along faults F10, F11, F12 and F7 in the southern part of the study area, and along faults F44 and F75 in the northern part. The white boxes indicate places were the strike of the TWT contour lines are discordant to the trends of the amplitude anomalies. **(b)** Seismic profile (cross line) orthogonal to F10 and H9. This section is displayed with 2 times vertical exaggeration. This anomaly becomes less bright near the highest point of the footwall of F10 (arrowed). Location of this section is shown in Figure 7a.

4.2.2. RMS amplitudes

The RMS amplitude map highlights similar features (Figure 8). Two RMS amplitude anomalies corresponding to the NNW-SSE and N-S trending features observed in the amplitude map (section 4.2.1) can be seen. Again, these features are discordant to the local TWT structure contours. There is also a region characterised by low RMS amplitudes (blue colours) within the hanging-wall of F10 that continues towards the southern edge of the study area and appears to be cross-cut by faults F22 and F41.

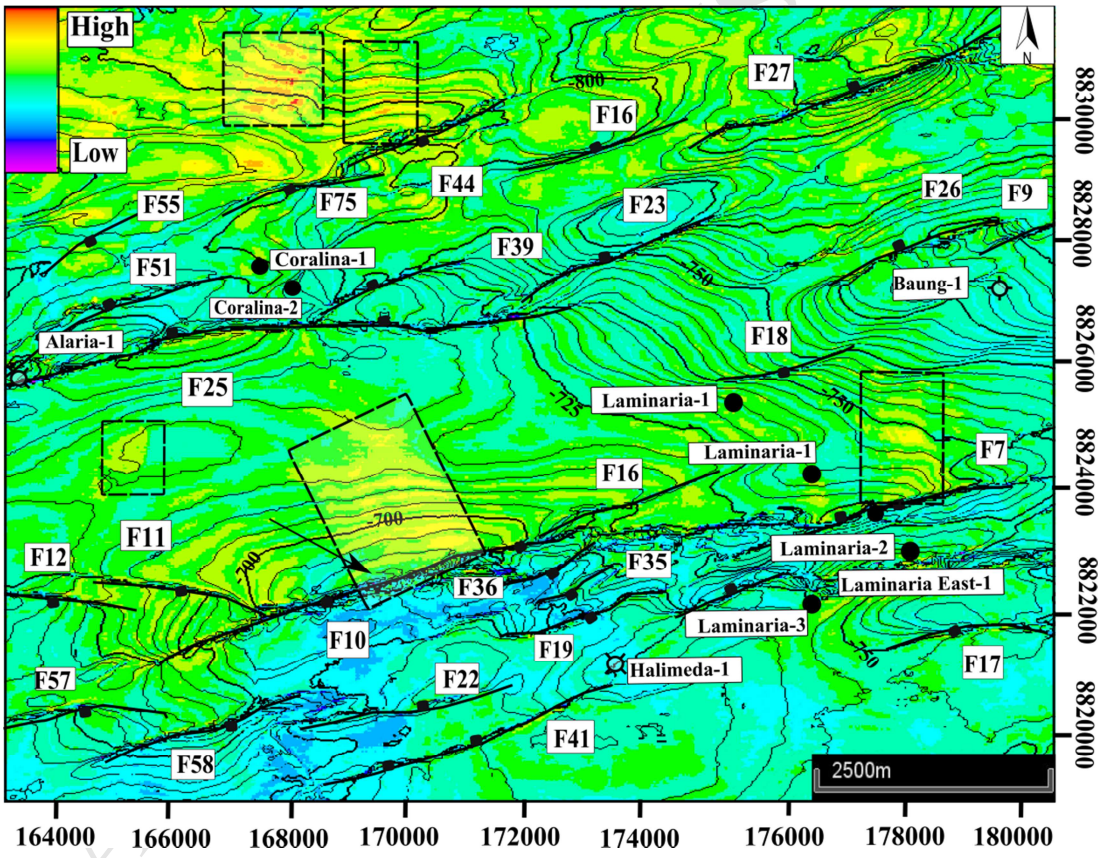

Figure.8. RMS amplitude map with two-way time structure contours for H9. The map shows high RMS amplitude anomalies associated with faults F7, F10 and F11 in the southern part of the study area and with faults F44 and F75 in the northern part of the study area.

4.3. Horizon H10

4.3.1. Amplitude and edge detection attribute

It was not possible to map H10 with confidence across the entire seismic survey area; we therefore focussed on the main region that shows the amplitude anomalies. Here, anomalies exist in both the footwall and hanging-wall of F10. In the footwall, the principal anomaly is elongated in a NW-SE direction and is discordant to the TWT structure contours.

The brightest anomaly occurs in the hanging-wall of F10 between two small-throw, minor faults F1 and F2 with maximum throws of approximately 15ms. These faults strike perpendicular to faults F10 (Figure 9a). A further anomaly occurs adjacent to the minor, NW-SE striking fault F3 (Figure 9a). F1, F2 and F3 are below the seismic resolution. Therefore, we use the edge detection filter on the seismic data. Along H10, this filter was able to highlight the major faults and structures and also many of the minor faults (Figure 9b), and shows the relationship between them. It is clear how the small throw faults (F1, F2 and F3) intersect the major faults (F22, F41, F57 and F58) at branch points on this horizon (Figure 9b).

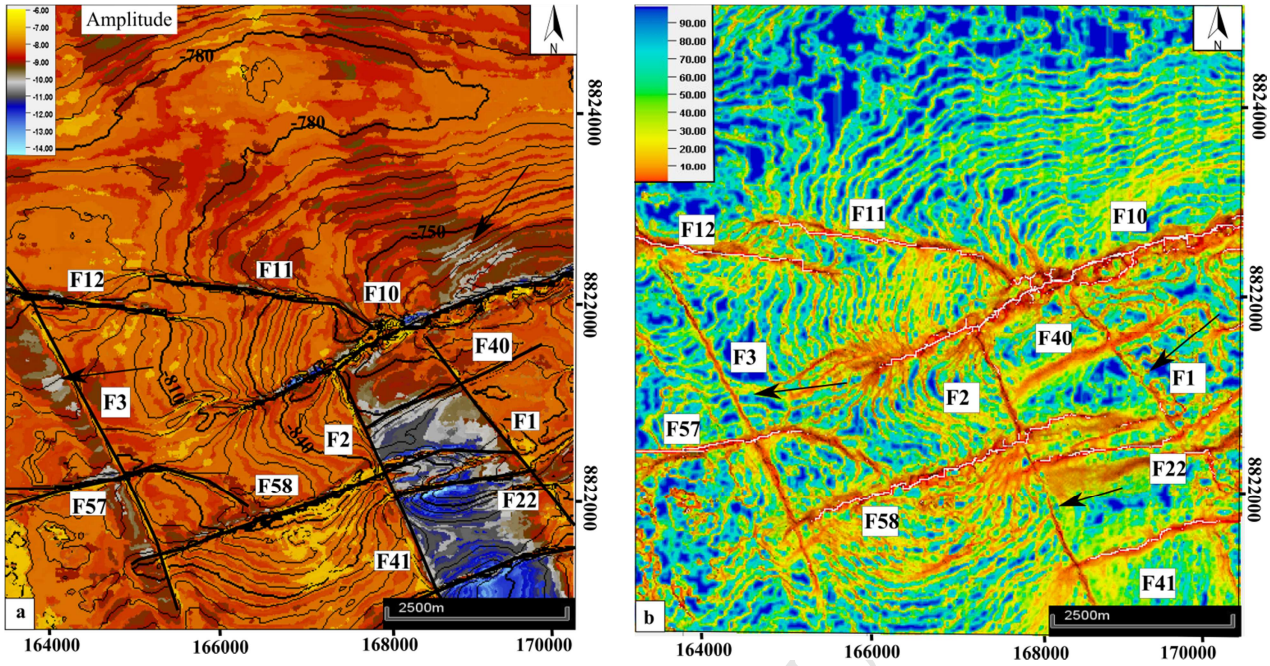

Figure 9. (a) Amplitude extraction map of H10, showing the two-way time structure contours. Note the high negative amplitude anomalies along F10, F22, F41 and F58 (blue and grey colours in the hanging walls of these faults). The distribution of these amplitude anomalies is controlled by three small-throw faults (F1, F2 and F3) that are perpendicular to F57, F58 and F22 respectively. **(b)** Edge detection map of H10 showing the three sets of minor faults, F1, F2 and F3, perpendicular to the major faults F10, F22, F41, F57 and F58 respectively. These minor faults are highlighted by black arrows.

4.3.2. RMS amplitudes

Anomalies shown on the RMS amplitude map (Figure 10) for H10 display similar trends and locations as the amplitude anomalies described above. The map shows the NW-SE elongation of the anomaly associated with F3, and the discordance between the anomaly and the local TWT structure contours (Figure 10-arrow). The RMS amplitude map again highlights the importance of the minor, small-throw faults in controlling the distribution of anomalies on H10.

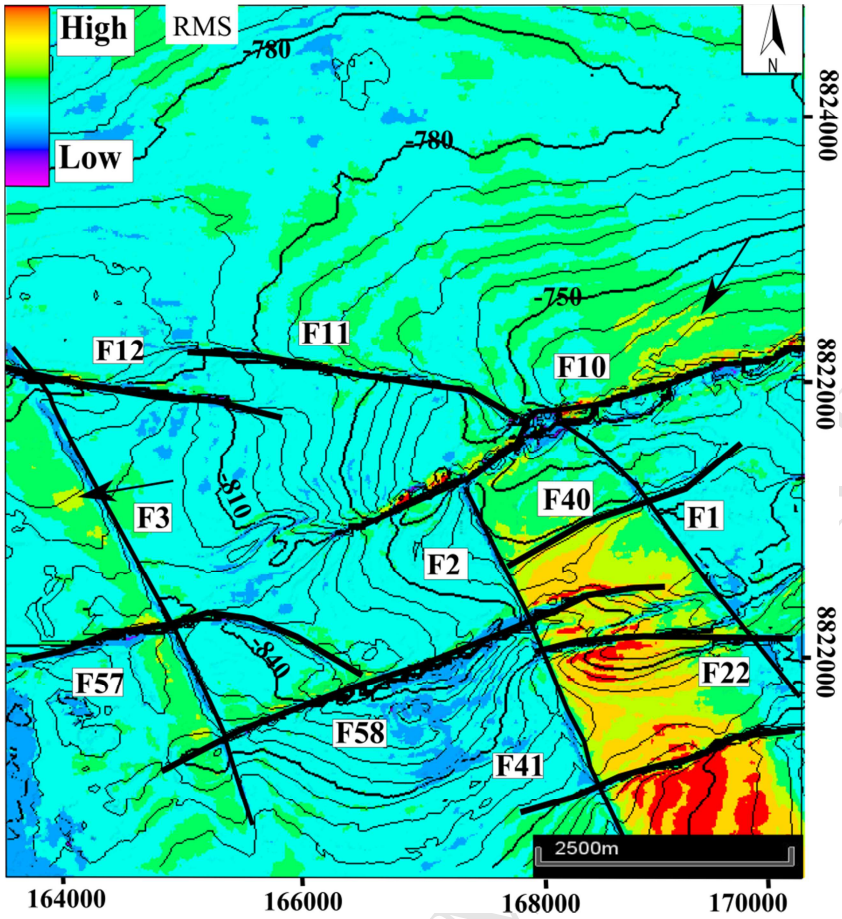

Figure .10. RMS amplitude map of H10 showing high RMS amplitude anomalies associated with faults F1, F2 and F3 in the NW-SE direction and with fault F10 in the E-W direction. Note the discordance between the anomalies along F3 and F10 and the local TWT structure contours as shown by arrows.

4.4. Horizon H13

4.4.1. Amplitude

The distribution of amplitude anomalies on along H13 is different to those observed on H9 and H10. For example, the anomaly associated with F10 is indistinct on this horizon (Figure 11). There is another set of anomalies that are elongated in N-S or NE-SW directions and appear to be cut by the fault traces. Overall, the amplitude map for H13 shows a change from predominantly orange colours in the west, to predominantly yellow colours in the east; however, the cause is unknown.

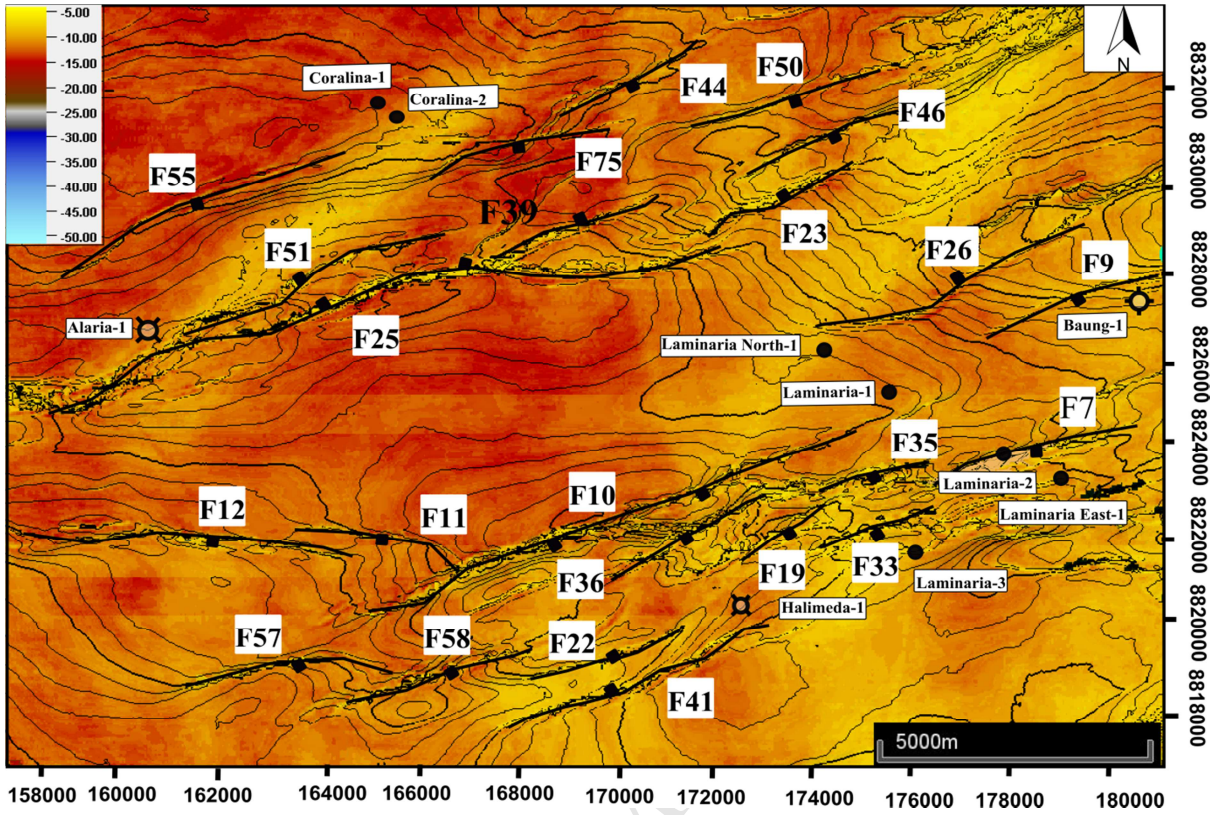

Figure 11. Amplitude extraction map for H13 showing the well locations and two-way time structure contours. The amplitude anomalies on this map have different distributions and are less distinctive compared to the amplitude anomalies on the shallower horizons.

2.4.4.2. RMS amplitudes

The RMS amplitude map highlights the N-S and NE-SW trending anomalies (Figure 2.12). These anomalies are oblique to the strike of the major faults and to the TWT structure contours, and appear to be cross-cut by the fault traces on H13.

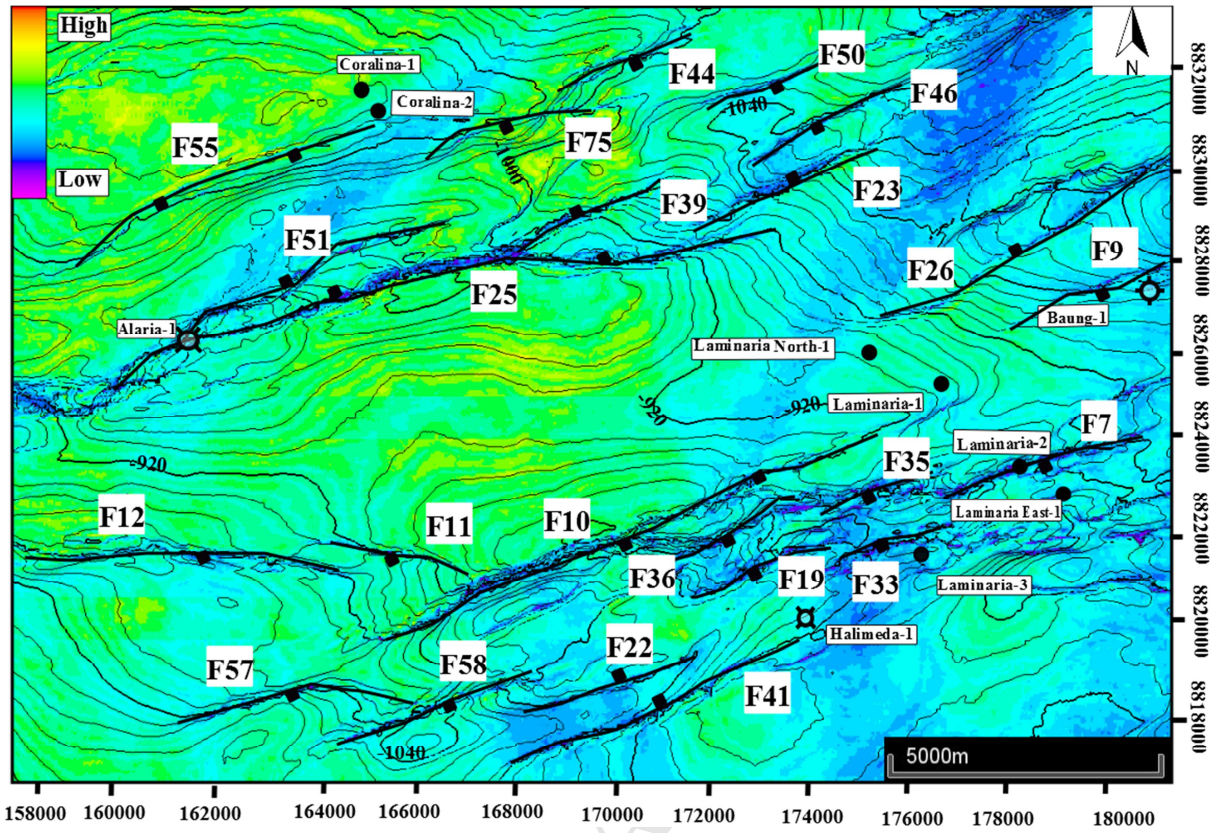

Figure 12. RMS amplitude map of H13 showing the two-way time structure contours; amplitude anomalies on this map have different distributions and are less distinctive to the amplitudes anomalies on the shallower horizons.

4.5. Timing and duration of fault activity

Gartrell et al. (2006) suggested that breached or partially-breached hydrocarbon traps at reservoir level (Laminaria Formation) develop where the reservoir is cut, or is bounded by vertically continuous, long-lived faults that link the reservoir with discharge sites at the seabed. Therefore, we might predict that amplitude anomalies are most likely to occur along faults that were active for the longest durations, and which cut the present-day seabed.

Figures 4 and 7 show that the majority of faults that cut H9 are also visible on the seabed amplitude and RMS anomaly maps. The exceptions are F44, F55 and F75 in Figure 7, which do not have a clear expression on the seabed (Figure 4). This observation suggests that the

majority of faults within our study area – including many of those that are associated with amplitude anomalies on the deeper horizons – are active at the present day.

We now constrain the *onset* of fault activity using the methodology described by Childs et al. (2003) (see section 3.2.2). For the purposes of this study, we need to identify the base of the syn-faulting sequence for different faults within the study area. The base of the syn-faulting sequence is defined as the oldest stratigraphic reflector that was deposited at the start of the period of activity (displacement) along an individual fault plane. The differences in fault throw measured on each successive syn-faulting horizon is a function of fault growth and sedimentation rate, provided sedimentation rates exceed fault throw rates (i.e. a growth fault; Childs et al., 1993, 2003). There is no evidence for erosion of footwall crests at the level of H9 or older horizons, nor is there evidence for significant channel development at shallower levels. We therefore assume that the condition that fault scarps were preserved by rapid burial has been met.

Figures 13 a, b and c show the throw-contoured strike projection maps of faults F11, F12 and F22, and the fault polygons along each intersecting horizon. These figures show that the boundary between the sub-vertical and sub-horizontal throw contours on each fault coincides approximately with horizon H9. Thus, H9 represents the base of the syn-faulting sequence. In other words, these faults became active at approximately the same time as the deposition of sediments associated with the H9 reflector, which we infer to have defined the sea-floor at that time. All these faults are visible on the seabed amplitude map (Figure 4), which indicates that they remain active at the present day.

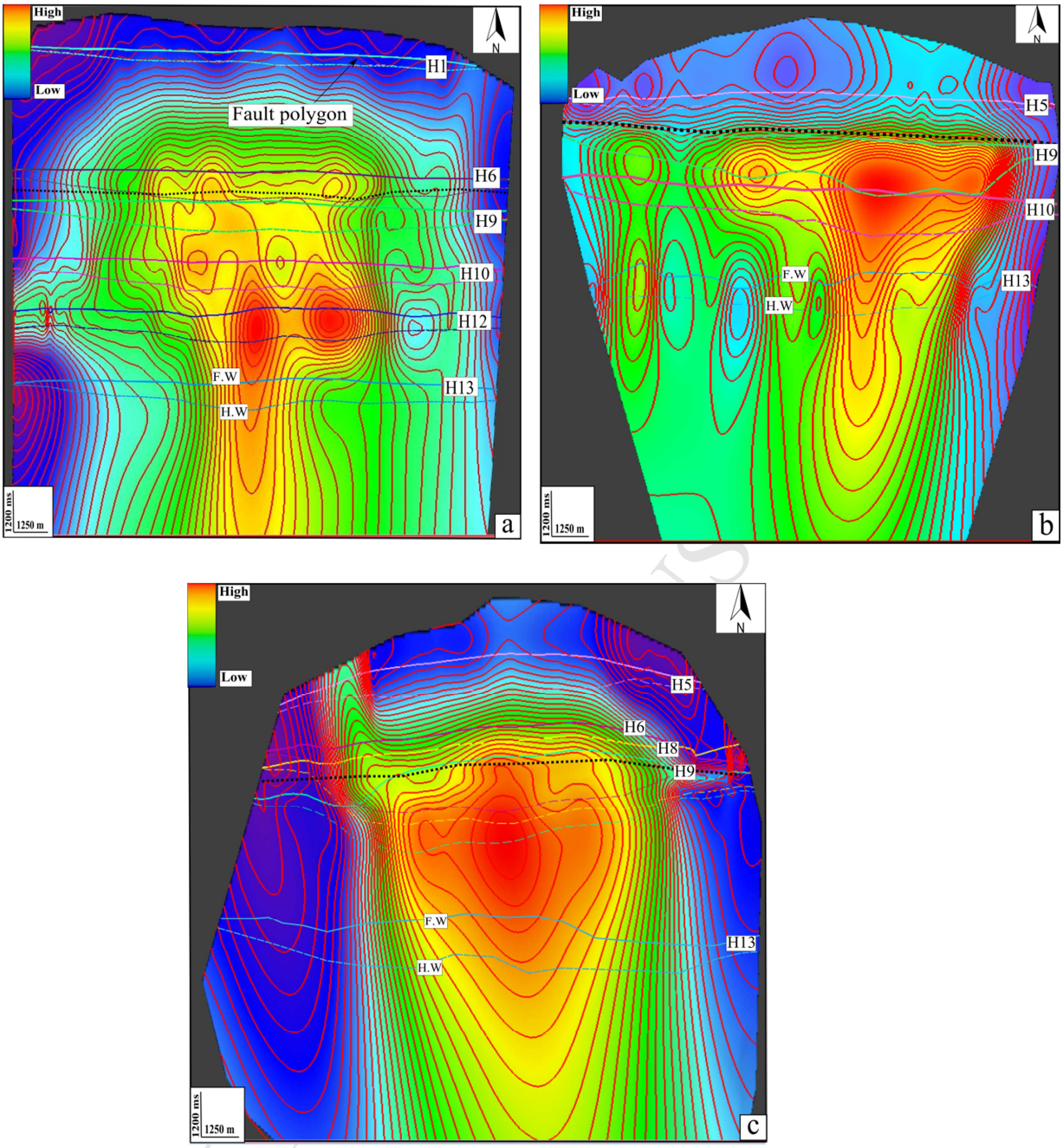

Figure 13 (a, b, and c). Throw-contoured strike projection maps of faults F11, F12 and F22, showing the intersections of each mapped horizon in the footwall and hanging wall of each fault. The black dotted line indicates the boundary between the pre- and syn-faulting sequences. Note that H9 is located approximately within this boundary were the contour lines change from sub-vertical to sub-horizontal.

5. Discussion

5.1 The distribution of amplitude and RMS anomalies on syn- and pre-faulting horizons

The results show that the seabed reflector and H9 – which represent the present-day seafloor and the palaeo-seafloor at the onset of Cenozoic faulting, respectively - are characterised by prominent amplitude and RMS amplitude anomalies that are associated with the mainly ENE-WSW striking faults. This observation is consistent with Langhi et al's (2010) finding (using a different seismic volume) that the reflectivity distribution of the near-seabed reflectors is controlled by the structural network.

In contrast, the amplitude and RMS amplitude anomalies on the oldest mapped pre-faulting horizon (H13) are oblique to the overall fault strike and appear to be cross-cut by the fault traces. These observations suggest that the anomalies on H13 are likely to be caused by features that pre-date faulting, and are not related to structural or tectonic processes. H10 is the shallowest horizon mapped within the pre-faulting succession and shows an association between the amplitude and RMS anomalies and the minor, NW-SE striking faults (F1, F2 and F3).

Overall, the results indicate that the distribution of amplitude anomalies on the two syn-faulting horizons (seabed and H9) is significantly different from that on the two pre-faulting horizons (H10 and H13). An important finding is that evidence for the structural control on the reflectivity distribution identified by Langhi et al. (2010) is most obvious on horizons that were deposited synchronous with activity on the ENE-WSW striking fault network.

2.5.2 Structurally-controlled seepage and cementation at the seabed and palaeo-seabed

The principal anomaly on the seabed reflector occurs on the hanging-wall side of F10 and is elongated parallel to the TWT structure contours (Figure 4). The trace of F10 can be observed

on the seabed amplitude map; however, F10 has no significant bathymetric expression on the sea floor (Figure 3). As a result, the seabed reflector in the hanging-wall of F10 lies *up*-dip of the fault trace. Similar geometries are associated with the smaller anomalies observed along F11 and F12 (Figure 4). A possible explanation is that buoyant fluids migrate upward along F10 towards the seabed. The fault cuts permeable strata immediately at and below the seabed. Seepage, fluid migration and associated authigenic carbonate cementation on the seafloor (e.g. Langhi et al., 2010) and within these permeable strata is then controlled by the regional dip of the seabed. In this model, the trace of F10 along the seabed acts as a linear source for fluid seepage (Figure 14a).

The principal amplitude anomalies on H9 occur within the footwalls of F7, F10, F11 and F12, but are discordant to the local TWT structure contours. Their distribution cannot be explained by processes that involve ongoing (present-day) migration of buoyant fluids. Nevertheless, analysis of the throw contours demonstrates that H9 was at the (palaeo-) sea floor at the onset of fault activity. We suggest that the onset of faulting may have triggered upward (re)migration of buoyant fluids, along faults that cut the Laminaria Formation reservoirs as suggested by Gartrell et al. (2006). By analogy with the anomalies preserved on the present-day seabed reflector, the fluids encountered poorly compacted, permeable strata at, and immediately below, the (palaeo-) sea floor (i.e. H9). Lateral migration of the fluids into these strata and along the palaeo-seafloor would have been up-dip towards local structural highs, such as (palaeo-) footwall crests (Figure 14b). The anomalies on H9 may result from the development of cemented hardgrounds that formed in response to hydrocarbon seepage at this time (Rollet et al., 2006; Figure14b). During subsequent burial, continued activity and possible growth/linkage along F10, F11, and F12 and nearby faults continued to modify the local subsurface structure. As a result, the hardgrounds were deformed and the associated anomalies are now discordant to the present-day TWT structure contours. In this model, the

anomalies observed on H9 are due to early diagenetic features (i.e. cemented hardgrounds), which effectively preserve evidence for fluid seepage at the palaeo-seabed. Detailed structural restoration of the evolving fault and horizon geometries is required to further test our proposal, but is beyond the scope of the present study.

5.3. Fluid migration, fault throw and the duration of fault activity

Our results show that the most prominent amplitude anomalies are associated with F10, which has a throw on H9 of approximately 100 ms, and with F7, F11, F12, which have throws of approximately 30 to 65 ms. In contrast, F25, which has a maximum throw of 108 ms along H9 does not have any significant associated anomalies. The duration of activity along these faults – with and without anomalies – is similar. Observations of the youngest pre-faulting horizon, H10, show that sub-seismic scale, NW-SE striking faults locally control the distribution of amplitude anomalies and the inferred locus of fluid migration and cementation. Thus, there is no direct relationship between fault size, or longevity, and fluid migration in the shallowest subsurface. Gartrell et al's (2006) trap integrity model suggests that remigration and loss of hydrocarbons from the Laminaria Formation occurred along large faults with high post-rift (Cenozoic) throws. The present results suggest that local variations in permeability – in addition to the structural configuration – played a significant role in controlling fluid migration and seepage in the shallowest subsurface, at or just below the seafloor/palaeo-seafloor.

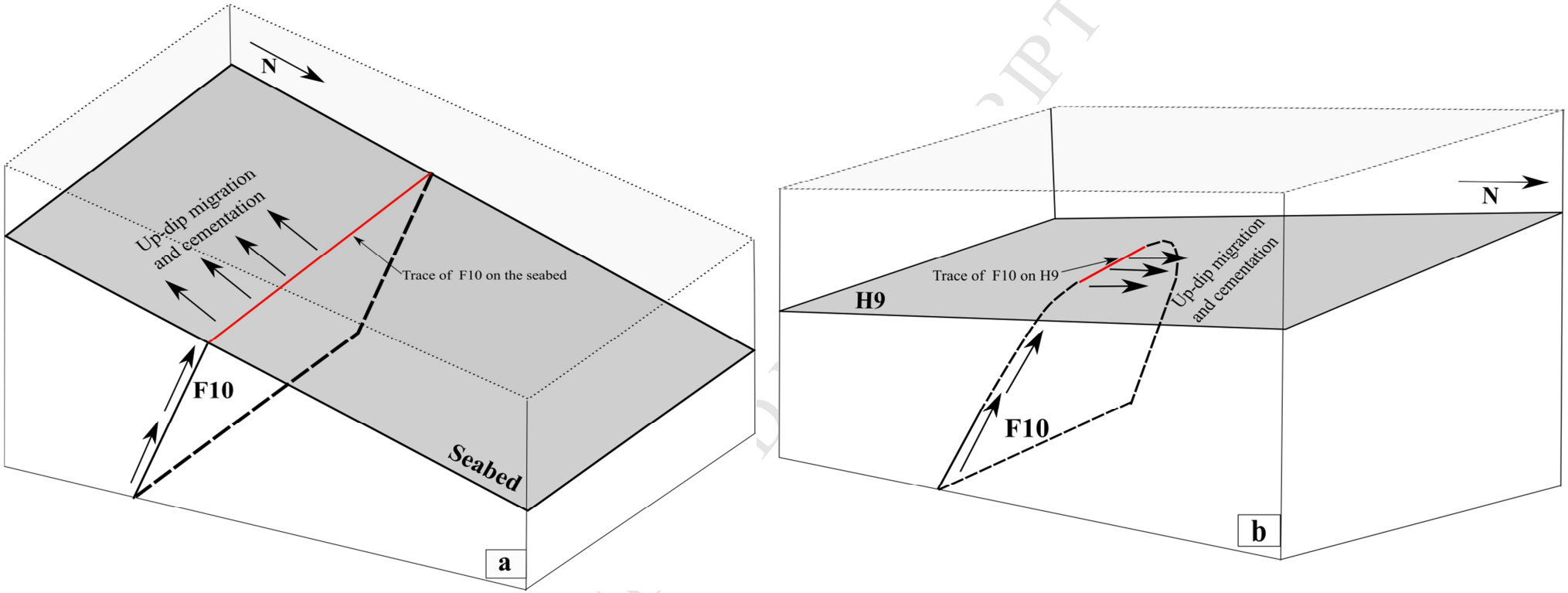

Figure 14. Schematic block diagrams showing the inferred migration of fluids upwards along F10, and seepage of fluids at the seafloor or palaeo-seafloor along the trace of F10 (red line). **(a)** Present day configuration of fault F10 and the seabed reflector, showing up-dip fluid migration and seepage and cementation on the seafloor; **(b)** Inferred configuration F10 and the palaeo-seabed (H9) at the time of fault initiation. Previous authors suggest that the Cenozoic faults, such as F10, propagated upwards from the underlying, Mesozoic rift system (Gartrell et al., 2006). As a result, we infer that the trace of F10 along the palaeo-seabed (H9) may have been shorter than the present-day fault length (cf. Long and Imber 2010).

6. Conclusion

In this study, interpretations of the amplitude and root mean square (RMS) anomalies and the three-dimensional structure are integrated in order to understand the structural controls on fluid migration on the Laminaria High. The key findings are that:

- prominent amplitude anomalies occur on horizons within the syn-faulting, Cenozoic succession. These anomalies are associated with mainly ENE-WSW striking faults, consistent with a structural control on their distribution;
- the most prominent amplitude anomaly on the present-day seabed reflector is elongated parallel to the trace of an ENE-WSW striking fault. The anomaly is located on the up-dip side of the fault trace, parallel to the two-way time (TWT) structural contours on the seabed. These observations are consistent with the anomalies having developed in response to structurally-controlled fluid seepage along, and up-dip migration away from the fault trace;
- the prominent amplitude anomalies on the oldest syn-faulting reflector, whilst located adjacent to fault traces, are discordant to the local TWT structural contours. These observations are consistent with structurally-controlled fluid seepage and cementation whilst the reflector was at the (palaeo-) seafloor; the resulting hardgrounds were subsequently buried and deformed during ongoing sedimentation and fault growth/linkage;
- the prominent amplitude anomalies on the youngest mapped pre-faulting reflector are located adjacent to sub-seismic scale, NW-SE striking faults. These observations are consistent with the small-scale faults having influenced fluid migration and cementation within the shallowest part of the pre-faulting succession;

- there is no clear relationship between the presence of structurally-controlled anomalies and the magnitude, or the duration, of movement along individual faults within the Cenozoic succession.

Acknowledgements

We thank the Higher Committee for Education Development (HCED) in Iraq for their financial support of the first author's project. Special thanks to the Geoscience Australia for providing the 3D seismic and well data: http://www.ga.gov.au/nopims. Schlumberger and Badley Geoscience Ltd. are thanked for providing academic licenses for Petrel and TrapTester/T7, respectively. Dave Stevenson and Matthew Hepburn are thanked for the IT support. The authors thank Alex Lăpădat for his support in using Petrel software. JI was part-funded by a Royal Society Industry Fellowship, held in collaboration with Badley Geoscience Ltd. and Geospatial Research Ltd. (grant reference IF120038).

References:

Abbassi, S., Primio, R., Horsfield, B., Edward, D., Volk, H., Anka, Z., George, S., 2015. On the filling and leakage of petroleum from traps in the Laminaria High region of the northern Bonaparte Basin, Australia. *Marine and Petroleum Geology*.59, pp.91–113. doi:S0264817214002554.

Baillie, P., Powell, C.M.A., Li, Z., Ryall, A., 1994. The tectonic framework of Western Australia's Neoproterozoic to Recent sedimentary basins. In: Purcell, P.G., Purcell, R.R. (Eds.), The Sedimentary Basins of Western Australia, Proceedings of the Petroleum Exploration Society of Australia Symposium. Perth, Western Australia, pp. 45-62.

Barnes, O.R., and Goldberg, E.D. 1976. Methane production and consumption in anoxic marine sediments. Geology, v. 4, no. 5, pp. 297-300.

Blumenberg, M., Walliser, E., Taviani, M., Seifert, R., and Reitner, J. 2015. Authigenic carbonate formation and its impact on the biomarker inventory at hydrocarbon seeps: A case study from the Holocene Black Sea and the Plio-Pleistocene Northern Apennines (Italy). *Marine and Petroleum Geology*, v. 66, pp. 532-541.

Brown, A.R. 2011. Interpretation of Three-Dimensional Seismic Data, seventh edition, AAPG, Memoir 42, SEG Investigations in Geophysics, no. 9, Tulsa, Oklahoma, USA.

Charlton, T.R., Barber, A.J., and Barkham, S.T. 1991. The structural evolution of the Timor collision complex, eastern Indonesia. *Journal of Structural Geology*, v. 13, pp. 489–500.

Childs, C., Easton, S.J., Vendeville, B.C., Jackson, M.P.A., Lin, S.T.,Walsh, J.J., Watterson, J., 1993. Kinematic analysis of faults in aphysical model of growth faulting above a viscous salt analogue.*Tectonophysics.* v.228, p.p.313–329.

Childs, C. Nicol, A., Walsh, J., Watterson, J., 2003. The growth and propagation of synsedimentary faults. J*ournal of Structural Geology*v. 25, pp.633–648.

Cowley, R., O'Brien, G.W., 2000. Identification and interpretation of leaking hydrocarbons using seismic data: a comparative montage of examples from the major fields in Australia's north west shelf and Gippsland Basin. Aust. Pet. Prod. *Explor. Assoc. J*, v.40, pp.121-15.

Gartrell, A., W. R. Bailey, and M. Brincat, 2005, Strain localisation and trap geometry as key controls on hydrocarbon preservationin the Laminaria High area: *APPEA Journal (Australian Petroleum Production and Exploration Association)*, v. 45, p. 477–492

Gartrell, A., Bailey, W.R. & Brincat, M., 2006. A new model for assessing trap integrity and oil preservation risks associated with postrift fault reactivation in the Timor Sea. *AAPG Bulletin*, v.90, pp.1921–1944.

Geoscience Australia, 2018. http://www.ga.gov.au/data-pubs, Accessed 05-06-2018.

George, S.C., Lisk, M., and Eadington, P.T. 2004. Fluid inclusion evidence for an early, marine-sourced oil charge prior to gas-condensate migration, Bayu-1, Timor Sea, Australia. Marine and Petroleum Geology., v. 21, pp. 1107-1128.

Hovland, M., Talbot, M.R., Qvale, H., Olaussen, S., and Aasberg, L. 1987. Methane-related carbonate cements in pockmarks of the North Sea. *Journal of Sedimentary Petrology*., v. 57, pp. 881-892.

Hovland, M. 1990. Do carbonate reefs form due to fluid seepage? *Terra Nova*, v. 2, pp. 8-18.

Hovland, M., Croker, P.F., and Martin, M. 1994. Fault-associated seabed mounds (carbonate knolls?) off western Ireland and north-west Australia. *Marine and Petroleum Geology*., v. 11, pp. 232-246.

Hovland, M. 2002. On the self-sealing nature of marine seeps. *Continental Shelf Research*., v. 22, pp. 2387-2394.

Howarth, V., and Alves, T.M. 2016. Fluid flow through carbonate platforms as evidence for deep-seated reservoirs in Northwest Australia. *Marine Geology* , v. 380, pp. 17-43.

Keep, M., Clough, M., and Langhi, L. 2002. Neogene tectonic and structural evolution of the Timor Sea region, NW Australia. In M. Keep and S. Moss, (eds) The sedimentary basins of Western Australia: *Proceedings of Petroleum Exploration Society of Australia Symposium*, 3, pp. 341–353.

Langhi, L. and Borel, G.D., 2008. Reverse structures in accommodation zone and early compartmentalization of extensional system, Laminaria High (NW shelf, Australia). Marine and Petroleum Geology.,v. 25, pp.791-803.

Langhi, L., Zhang, Y., Gartrell, A., Underschultz, J., Dewhurst, D.,2010. Evaluating hydrocarbon trap integrity during fault reactivation using geomechanical three dimensional modelling : An example from the Timor Sea, Australia. *AAPG BULLETN*.94(4), PP.567-591.doi:10.1306/10130909046.

Langhi, L., Ciftci, N.B., and Borel, G.D. 2011. Impact of lithospheric flexure on the evolution of shallow faults in the Timor foreland system. *Marine Geology*., v. 284, pp. 40-54.

Long, J.J., Imber, J., 2010. Geometrically coherent continuous deformation in the volume surrounding a seismically imaged normal fault-array. *Journal of Structural Geology*, v.32, pp.222-234.

Long, J.J., Imber, J., 2012. Strain compatibility and fault linkage in relay zones on normal faults.*Journal of structural Geology.* 36, pp.16-26.

Luo, Y., Higgs, W.G., Kowalik, W.S., 1996. Edge detection and stratigraphic analysis using 3D seismic data. SEG 1996 Expanded Abstracts. 324–327.

Løseth, H., Gading, M., Wensaas., L., 2009. Hydrocarbon leakage interpreted on seismic data. Marine and Petroleum Geology. 26, pp. 1304-1319.

O'Brien, G. W., M. Lisk, I. R. Duddy, J. Hamilton, P. Woods, andR. Cowley, 1999, Plate convergence, foreland developmentand fault reactivation: Primary controls on brine migration,thermal histories and trap breach in the Timor Sea, Australia:Marine and Petroleum Geology, v. 16, p. 533– 560.

O'Brien, G.W., and Woods, E.P., 1995. Hydrocarbon-related diagenetic zones (HRDZs) in the Vulcan Sub-basin, Timor Sea: recognition and exploration implications. APEA Journal, v. 35, pp. 220–52.

O'Brien, G. W., M. Lisk, I. R. Duddy, J. Hamilton, P. Woods, andR. Cowley, 1999, Plate convergence, foreland developmentand fault reactivation: Primary controls on brine migration,thermal histories and trap breach in the Timor Sea, Australia: Marine and Petroleum Geology, v. 16, p. 533– 560.

O'Brien, G.W., Glenn, K., Lawrence, G., Williams, A., Webster, M., Burns, S., Cowley, R., 2002. Influence of hydrocarbon migration and seepage on benthic communities in the Timor Sea, Australia. *APPEA Journal*, v. 42,pp. 225–240.

Othman, A.A.A., Fathy, M. & Maher, A., 2016. Use of spectral decomposition technique for

delineation of channels at Solar gas discovery, offshore West Nile Delta, Egypt.pp.45–51.

Rollet, N. Logan, G.A., Kennrad, J.M., O'Brien., Jones, A.T., Sexton., 2006. Characterisationand correlation of active hydrocarbon seepage using geophysical data sets: An example from the tropical, carbonate Yampi Shelf, Northwest Australia. Marine and Petroleum Geology, 23(2), pp.145–164, doi: S0264817205001273.

Partyka, G., J. Gridley, J., Lopez, 1999, Interpretational applications of spectral decomposition in reservoir characterization: The Leading Edge.18(3), p. 353–354,doi:10.1190/1.1438295.Brown, a R., 1999. Interpretation of Three-Dimensional Seismic Data. *AAPG Memoir*, (9), pp.1–528.

Ruig, M.J. De et al., 2000. Fault architecture and the mechanics of fault reactivation in the Nancar Trough/Laminaria area of the Timor Sea. *APPEA Journal*, pp.174–193.

Shuster, M.W., Eaton, S., Wakefield, L.L. and Kloosterman, H.J., 1998. Neogene tectonics, greater Timor Sea, offshore Australia: Implications for trap risk. APPEA Journal (Australian Petroleum Production and Exploration Association), v. 38, pp.351-379.

Simm, R.,Bacon,M.,2014.Seismic Amplitude:An Interpreter's Handbook.Cambridge University Press.

Smith, G.C., Tilbury, L.A., Chatfield.A, Senycia, and P,Thompson, N.,1996. Laminaria - A new Timor Sea discovery: *Australian Petroleum Production and Exploration Association Journal*, v. 36, no. 1, pp.12-28.

Whittam, C.B., Norvick, M.S., Mclntyre, C.L., 1996. Mezozoic and Cainozoic tectonstratigraphy of Western ZOCA and adjacent areas.*Australian Petroleum Production andExplorationAssociationJournal*,v.36,no.1,pp209-231.

Van Tuyl, J., Alves, T.M., Cherns, L. 2018. Pinnacle features at the base of isolated carbonate buildups marking point sources of fluid offshore Northwest Australia, doi.org /10.1130/B31838.1.

Highlights

- Amplitude anomalies are associated with active faults.
- The distribution of anomalies differs on syn- and pre-faulting horizons.
- The anomalies result from cementation at the seafloor and palaeo-seafloor.
- Sub-seismic scale structures influence fluid migration in the shallow subsurface.